Applied Physics A (2023) 129:487
https://doi.org/10.1007/s00339-023-06745-4

Applied Physics A
Materials Science & Processing

Crystallization process, microstructure, thermal behavior, and magnetic properties of melt-spun $Fe_{86}Cr_6P_6C_2$ ribbons

L. Abadlia[1,2] · M. I. Daoudi[3,4] · S. Alleg[3]

Received: 23 February 2023 / Accepted: 26 May 2023

Abstract
The crystallization process, microstructure, thermal stability, and magnetic properties of $Fe_{86}Cr_6P_6C_2$ amorphous ribbons were studied by X-ray diffraction, scanning electron microscopy coupled with energy dispersive X-ray spectroscopy, differential scanning calorimetry, and vibration sample magnetometry. The crystallization process occurs in three stages where nanocrystalline α-Fe solid solution, Fe_3P phosphide, θ-Fe_3C and ε-Fe_3C carbides are formed. The crystallite size increases with increasing annealing temperature and remains at the nanometer scale (20–88 nm). The microstructure of the annealed ribbons consists of lamella, fine platelets, alternate planes of ferrite and cementite, and grains with different shapes and sizes. The activation energies (499, 386, and 369 kJ/mol) are determined by Kissinger method. The melt-spun ribbons exhibit a low coercivity of 16.598 Oe and a high saturation magnetization of 0.635 emu compared to the annealed ones. The saturation magnetization decreases to a minimum value for the annealed ribbons at 758 K and then increases with increasing the annealing temperature. The Curie temperature increases from 447.4 K for the melt-spun ribbons to 638 K for the fully crystallized ribbons due to the development of the α-Fe phase.

Keywords Fe–Cr–P–C alloys · XRD · Thermal stability · Crystallization kinetics · Magnetic properties

1 Introduction

Iron-based amorphous alloys or metallic glasses have received increasing attention over the last decades due to their excellent magnetic properties, strength, hardness, wear and corrosion resistance, electrochemical properties, and low cost [1–9]. Furthermore, compared with traditional crystalline alloys, Fe-based amorphous alloys showed higher efficiency in degrading organic pollutants in wastewater (azo dyes) due to their short-range order and long-range disorder atomic structures [10].

Amorphous alloys are characterized by short-range atomic order, non-uniform distribution of free volume, and non-equilibrium thermodynamic state. Consequently, they undergo structural relaxation or a more stable energy state when annealed at temperatures well below the glass-transition temperature (T_g). Structural relaxation affects chemical short-range atomic order (CSRO) and topological short-range atomic order (TSRO). CSRO, which is associated with a change in the order of atoms of a given type, can be reversible or irreversible. In contrast changes in TSRO are irreversible due to the reduction in and redistribution of free volume [11, 12]. Likewise, nanocrystalline (NC) materials derived from amorphous alloys show improved physical, mechanical, magnetic, magnetocaloric, and chemical properties, such as excellent catalytic properties, superior hardness, high strength, and unusual thermal properties [13–19]. Furthermore, amorphous/NC alloys exhibit improved thermal stability and ductility which are difficult to achieve with amorphous and NC alloys [20, 21].

Various methods were used to produce iron-based amorphous/NC alloys, such as mechanical alloying,

✉ L. Abadlia
Eabadlia_lakhdar@yahoo.fr

[1] Department of Material Sciences, Faculty of Sciences and Technologies, University of Mohamed Cherif Messaadia, 41000 Souk Ahras, Algeria

[2] Laboratory of Inorganic Materials Chemistry (LIMC), Badji Mokhtar-Annaba University, Annaba, Algeria

[3] Laboratoire de Magnétisme et Spectroscopie des Solides (LM2S), Badji Mokhtar Annaba University, BP 12, 23000 Annaba, Algeria

[4] Department of Science of Matter, Faculty of Mathematics and Computer Science and Material Science, University 8 Mai 1945, 24000 Guelma, Algeria

Published online: 14 June 2023

melt-spinning, electrodeposition, sputtering, severe plastic deformation, crystallization of amorphous alloys, and injection-casting method [22–29]. Fe-based amorphous alloys were produced on a large scale in the industry to produce various types of equipment, instruments manufacture, mechanical engineering and high-precision devices such as data carriers, magnetic sensors, security systems, and high-efficiency transformers [30–33]. Nearly all the compositions that produce stable amorphous structures at room temperature (RT) contain approximately 80 at.% of the transition metals (Fe, Cr, Co, Ni, etc.). Due to their good magnetic properties [34–36], amorphous FeCrPC and FeCrPCSi ribbons can be used in many industrial applications such as magnetic shielding due to their high permeability, electromagnetic marking (anti-theft marking, recognition in concretes, paints, etc.), and composite conductors' (protection against electrostatic discharge). Furthermore, Fe–P–Cr–C alloys exhibit outstanding mechanical properties and high corrosion resistance in neutral and acid solutions [37, 38]. For example, the hardness of Fe–Cr–P–C nanoamorphous coatings (850–950 kg/mm^2) is nearly two times higher than that of stainless steels [39]. Consequently, they are intended for structural use to contribute to the load-bearing capacity of a concrete element or grout, including concrete or shotcrete, paving concrete, precast concrete, cast-in-place concrete and concrete or repair [40, 41]. In such application, the amorphous cut melt-spun ribbons are mixed with concrete to reinforce it. Therefore, knowledge of crystallization laws and parameters measured at high temperatures allows extrapolating, for lower temperatures, the foreseeable crystallization times of the alloy. The alloys properties can be influenced by the preparation conditions and their performance can be strongly interrelated to their microstructure. Furthermore, it is well known that the heat treatment of amorphous ribbons near the crystallization onset leads to structural relaxation and affects significantly their structural, microstructural, and magnetic properties. Consequently, it is important to understand and control their crystallization process to attain optimum microstructures and control their useful operating temperature range for specific technological applications. Most studies on amorphous Fe–Cr–P–C ribbons, wires, and coatings have focused on mechanical and magnetic properties [34, 36, 37, 42]. The present work aims to investigate the crystallization behavior, structural (phase formation) and microstructural changes, thermal stability, and magnetic properties of the melt-spun $Fe_{86}Cr_6P_6C_2$ ribbons deeply as a function of the annealing temperature using of X-ray diffraction (XRD), scanning electron microscopy (SEM) coupled with energy dispersive X-ray spectrometry (EDX), differential scanning calorimetry (DSC), and vibrating sample magnetometry (VSM).

2 Experimental details

Industrial amorphous $Fe_{86}Cr_6P_6C_2$ (wt.%) ribbons were supplied by the Saint-Gobain SEVA Company (France). The amorphous ribbons (~ 59 µm in thickness and 1–2 mm in width) were prepared by melt-spinning onto a steel wheel under argon atmosphere [43]. The crystallization process was monitored as changes in heat flow by differential scanning calorimetry (DSC) in a DSC SETARAM 131 instrument, under argon atmosphere, at different heating rates of 5, 10, 20, and 30 K/min. The annealing temperatures relating to different crystallization stages, in the range of 673–973 K, were determined from the DSC curve measured with a heating rate of 10 K/min. The melt-spun ribbons were sealed into quartz tubes under 10^{-3} mbar vacuum and subjected to annealing in a muffle furnace, at a heating rate of 10 K/min, kept for approximately 2 min at different temperatures (729, 761, and 873 K), and then quenched into water. The morphology of the melt-spun and annealed ribbons was followed by a TESCAN Vega 3 Scanning Electron Microscope (SEM) equipped with energy dispersive X-ray spectrometry (EDX). The phase formation during the crystallization process was examined by X-ray diffraction (XRD) on a PANalytical Empyrean diffractometer with a CuK_α radiation ($\lambda = 1.54056$ Å). The measurements were performed in a θ–θ Bragg Brentano geometry over a 2θ range from 10 to 120° with a step size of 0.013°. The Rietveld refinement of the XRD patterns was performed by using the MAUD program [44] which is based on the Rietveld method [45]. The variation in the magnetization as a function of the applied magnetic field, $M(H)$, was carried out by a vibrating sample magnetometer (VSM) LakeShore 7404, at room temperature, under an external magnetic field of 10 kOe. Temperature dependence magnetization curves, $M(T)$, were measured in the temperature range of 298–873 K under an applied magnetic field of 6 kOe by a MicroSense magnetometer.

3 Results and discussion

3.1 Thermal and microstructural characterizations

As they are thermodynamically unstable, the amorphous alloys transform to a more relaxed structural state where a short-range atomic order (SRO) occurs upon heating below the crystallization temperature. Because the crystallization process is thermally activated, several properties of the alloy change irreversibly or reversibly. DSC is a practical, simple, and available thermal analysis method for characterizing different events and parameters such as,

the phase transition, crystallization process, temperature crystallization, crystallization kinetics, Curie temperature (T_C), glass transition temperature (T_g), and enthalpy transformation. At a constant heating rate, the DSC scan provides accurate and fast determination of T_C.

The DSC curves of the amorphous $Fe_{86}Cr_6P_6C_2$ ribbons at different heating rates (5, 10, 20, and 30 K/min) show three exothermic peaks related to three crystallization stages (Fig. 1). The weak exothermic shoulder to the right of the main exothermic peak is due to the overlap of two crystallization steps. This event complicates the crystallization analysis due to slight differences in crystallization temperature peaks. The shift of the DSC peaks to higher temperatures indicates that the crystallization process is thermally activated, and as the heating rate increases the atoms do not have sufficient time to locate the crystallization sites. Such

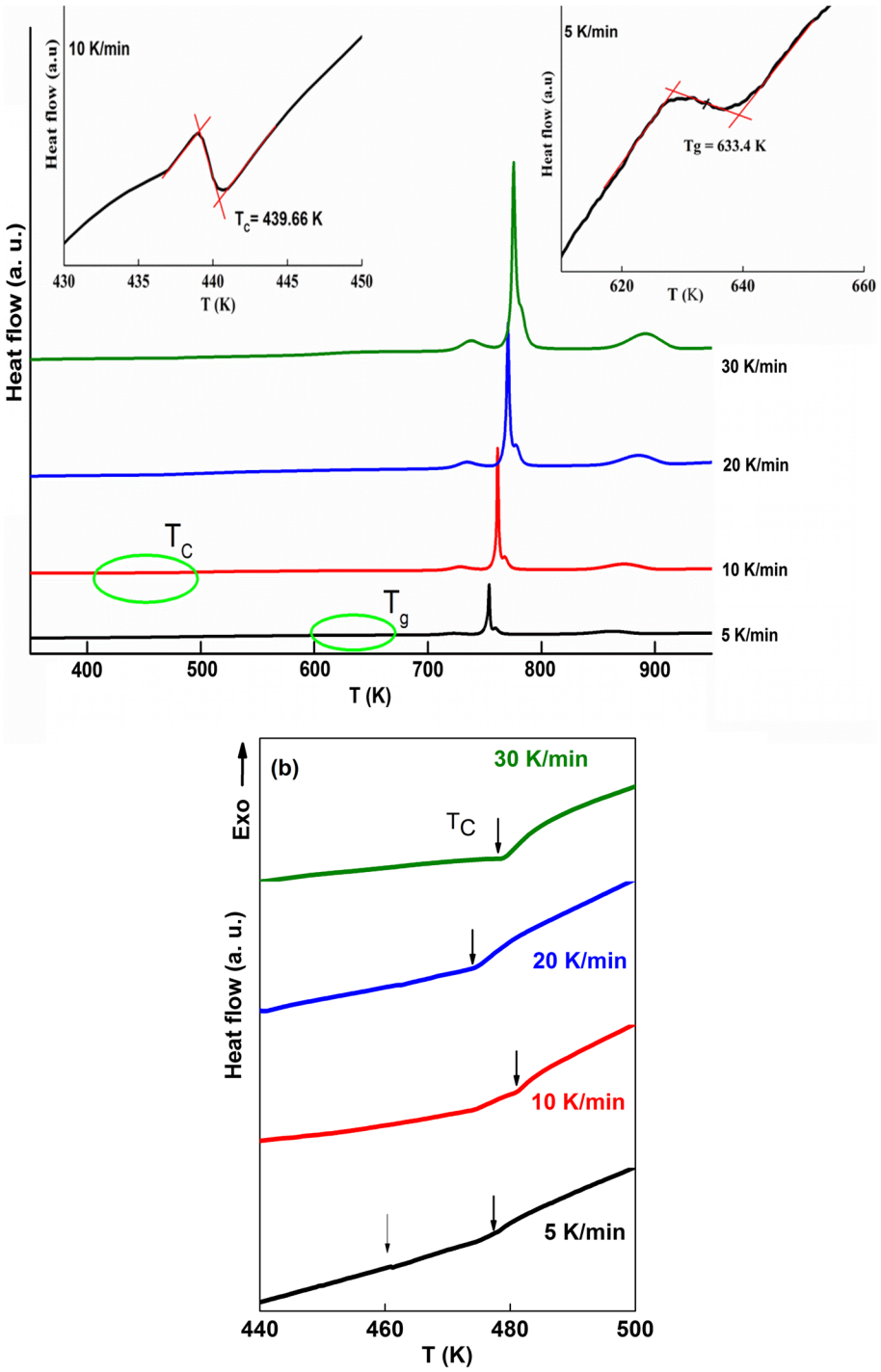

Fig. 1 DSC curves of the $Fe_{86}Cr_6P_6C_2$ ribbons as a function of heating rates

behavior is usually observed during the crystallization process of the amorphous alloys [46–49].

The endothermic peak that appears at approximately 638 K for the smaller heating rate (5 K/min) can be related to the glass transition, T_g, which is a pure dynamic phenomenon (inset in Fig. 1). Indeed, T_g is a kinetic event that depends on the experimental time scale and system reorganization. At a low temperature, a broad, fat exothermic peak appears before the T_g temperature can be observed in the DSC signal at a constant heating rate as an endothermic hump prior to the exothermic event. The onset temperature (T_x), peak temperature (T_p), offset temperature (T_e), and crystallization enthalpy (ΔH) for the annealed ribbons at different heating rates are summarized in Table 1. The line break in the DSC curves [50] at approximately 475 K can be attributed to the Curie temperature (T_C) of the amorphous phase (inset in Fig. 1, and Fig. 1b). The endothermic peak below T_C is related to the required energy for randomization in the ribbons' magnetic dipoles. In contrast, the exothermic peak appears afterwards T_C because no more energy is required for randomization. The value of T_C is higher than those reported earlier for the amorphous $Fe_{67}Cr_{7.3}P_{13.7}C_{9.5}Si_{2.5}$ (455 K) and $Fe_{71.1}Cr_{7.9}P_{11.2}C_{8.1}Si_{1.7}$ (419 K) ribbons [34]. Those discrepancies may be related to the structural state, CSRO of the amorphous structure, and alloy composition. Indeed, T_C depends on the heating rate and the cooling rate that influences the structure forming. Furthermore, it is highly sensitive to stress and relaxation [50].

Figure 2a shows the XRD patterns of melt-spun and annealed ribbons at different temperatures. The broad-angle peak around $2\theta = 40°–50°$ confirms the amorphous character of the ribbons. Besides, the difference in the intensity of the halo of the wheel and free sides (not shown here) can be related to the difference in the residual stress between the two side surfaces. Moreover, the average crystallite size is relatively higher at the free side with lower cooling rate as compared to that of the wheel side with faster cooling rate. The melt-spun ribbons present a crystallite size refinement, directional growth (texture), structural disorder (heterogeneities), high level of internal stresses and, in general, show a dissymmetry of shape and properties between the free and wheel sides. For the annealed ribbons at 729 K (An-729 K), the XRD pattern shows a very small peak superimposed to the broad halo indicating the formation of NC precipitates of α-Fe-type. The apparition of new diffraction peaks with increasing the annealing temperature is related to the formation of new phases. However, the disappearance of some diffraction peaks upon annealing at 873 K, as indicated by arrows in Fig. 2b, confirms the formation of a metastable phase during the second stage of crystallization (An-761 K). Based on those observations, the Rietveld refinement was performed by using different phases (Fig. 3): cubic α-Fe (space group *Im–3m*, lattice parameter $a_0 = 0.2862$ nm), tetragonal Fe_3P (space group *I-4*, lattice parameters $a_0 = 0.9106$ nm and $c_0 = 0.4465$ nm), orthorhombic cementite or θ-Fe_3C (space group *Pnma*, lattice constants $a_0 = 0.5079$ nm, $b_0 = 0.6730$ nm, and $c_0 = 0.4517$ nm), and hexagonal ε-Fe_3C carbide with lattice constants of $a_0 = 0.4767$ and $c_0 = 0.4354$ nm, and space group $P6_322$ [51]. The hexagonal form of cementite is less stable than the orthorhombic form. According to the XRD results (Table 2), the crystallization sequence of $Fe_{88}P_6Cr_6C_2$ amorphous alloy occurs as follows: amorphous structure $\rightarrow$ α-Fe + residual amorphous phase (at 729 K) $\rightarrow$ α-Fe + Fe_3P + θ-Fe_3C + ε-Fe_3C (at 761 K) $\rightarrow$ α–Fe + Fe_3P + θ-Fe_3C (at 873 K). The crystallization steps and, principally, the intermediate crystallization product can be affected mainly by the alloy composition. Indeed, a similar crystallization process was observed in the $Fe_{80}P_9B_2C_9$ amorphous alloy, where the α–Fe precipitated at 708 K, whereas Fe_3P and Fe_3C phases were formed at 780 K

Table 1 Values of temperature, enthalpy, and activation energy of the crystallization peaks at different heating rates

Peak	T (K)	Heating rate (K/min)				E_a (kJ/mol)
		5	10	20	30	
1	T_{x1}	699	704	710	714	
	T_{p1}	722	729	734	738	499.52 ± 6.31
	T_{e1}	739	747	755	759	
	ΔH_1 (*J/g*)	8.77	10.51	10.72	11.09	
	T_{x2}	742	748	758	762	
2	T_{p2}	754	761	771	775	386.38 ± 9.83
	T_{e2}	766	777	784	796	
	ΔH_2 (*J/g*)	46.34	64.52	57.73	56.78	
	T_{x3}	818	820	840	843	
3	T_{p3}	862	873	886	891	368.91 ± 12.75
	T_{e3}	895	908	918	926	
	ΔH_3 (*J/g*)	39.67	38.08	35.65	35.22	

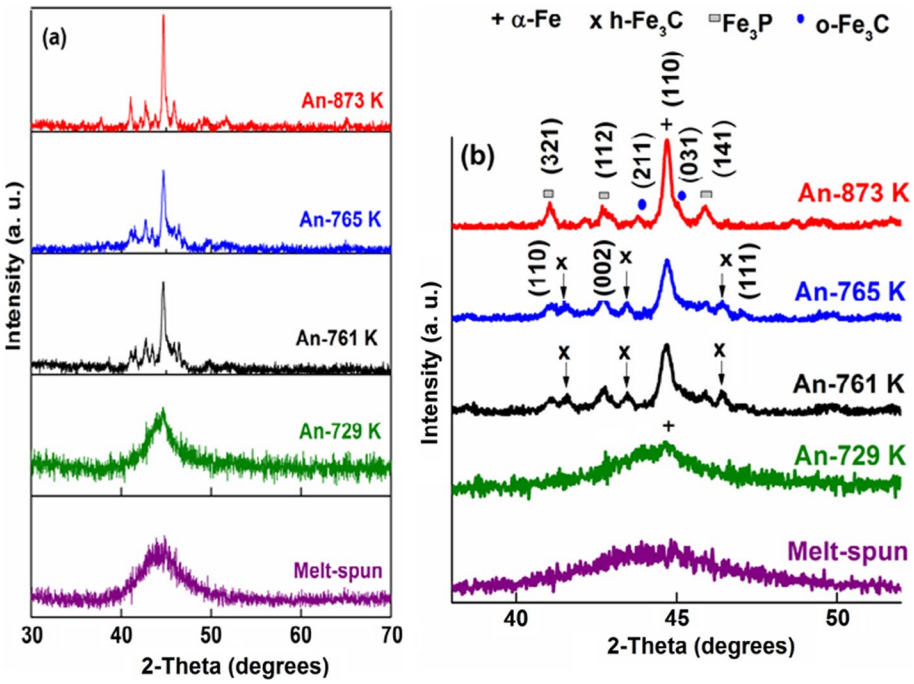

Fig. 2 **a** XRD patterns of the melt-spun and annealed ribbons at different temperatures, and **b** the evolution of the main diffraction peak

[35]. However, the crystallization of the $Fe_{77}Cr_4P_8C_{11}$ amorphous alloy proceeded by a two-step crystallization behavior where α-Fe and metastable Fe_7C_3 carbide were observed in the first stage, α-Fe, Fe_3P phosphide, and Fe_3C carbide were obtained in the second stage [25].

Chromium forms usually solid solutions (SS) with iron through the partial substitution of iron atoms for chromium atoms. Furthermore, owing to its strong affinity for carbon, chromium makes the cementite more stable when it is alloyed in $((Fe, Cr)_3C)$ and the free energy of formation decreases systematically with concentration [52]. Likewise, Fe ($r_{Fe}=0.126$ nm), Cr ($r_{Cr}=0.128$ nm), and P atoms ($r_P=0.128$ nm) show small differences in their atomic radii. Consequently, the formed phases can be considered as α-Fe(Cr) SS, Fe_3P-type phosphide, θ-Fe_3C-type and ε-Fe_3C-type carbides. According to the binary Fe–C phase diagram [53], the cementite or θ-Fe_3C carbide can be obtained at lower carbon content (<6.7%), while very few carbon atoms can form a solid solution with α-Fe (ferrite) in an equilibrium state. Besides, the higher diffusivity of C into the α–Fe matrix and its small atomic radius ($r_C=0.07$ nm) give rise to the formation of an interstitial solid solution. In the hexagonal ε-Fe_3C carbide, C atoms may be distributed among the octahedral interstices of Fe atoms, though the regularity of their distribution does not spread over the whole crystal matrix [51]. The unit cell contains six iron atoms and six octahedral interstitial sites, two of which are occupied by carbon atoms, resulting in a stoichiometry of Fe_3C. It has been reported that the hexagonal close-packed iron carbide is unstable and decomposes below 708 K [54]. This may explain the disappearance of some diffraction peaks in the XRD patterns, while the difference in the decomposition temperature may be related to the preparation conditions.

The variation in the crystallite size of the different phases as a function of annealing temperature is shown in Fig. 4. The crystallite size increases with increasing the annealing temperature and remains at the nanometer scale (20–88 nm). The weight fractions of α-Fe solid solution and θ-Fe_3C-type phases exhibit antagonist behaviors between 761 and 873 K (Fig. 5), while that of Fe_3P-type decreases from 46%, at 761 K, to ~ 38%, at 765 K, and levels off. One supposes that almost phosphorous atoms contribute to the formation of Fe_3P-type phosphide, while carbon atoms move between the α-Fe-type SS and θ-Fe_3C-type carbide structures.

The lattice parameter of the α-Fe(Cr) SS fluctuates slightly between 0.28641 and 0.28658 nm, while the lattice constants of Fe_3C-type and Fe_3P-type exhibit a contraction/expansion (Table 2). The relative deviances of the lattice constants from those of the powder diffraction file can be calculated as follows:

$$\frac{\Delta a}{a}=\frac{(a-a_0)}{a_0}\quad \frac{\Delta b}{b}=\frac{(b-b_0)}{b_0}\quad \frac{\Delta c}{c}=\frac{(c-c_0)}{c_0}, \qquad (1)$$

where a, b, and c are the lattice parameters of the annealed sample, while a_0, b_0, and c_0 are those of the perfect crystal. One notes that the relative deviation of the lattice parameter of the α–Fe-type phase varies between – 0.024 and – 0.083%. The contraction of the crystal lattice can be related to the diffusion of carbon atoms with a smaller atomic radius leading to the formation of a ferritic SS. Furthermore, the contraction/expansion of the crystal lattice of

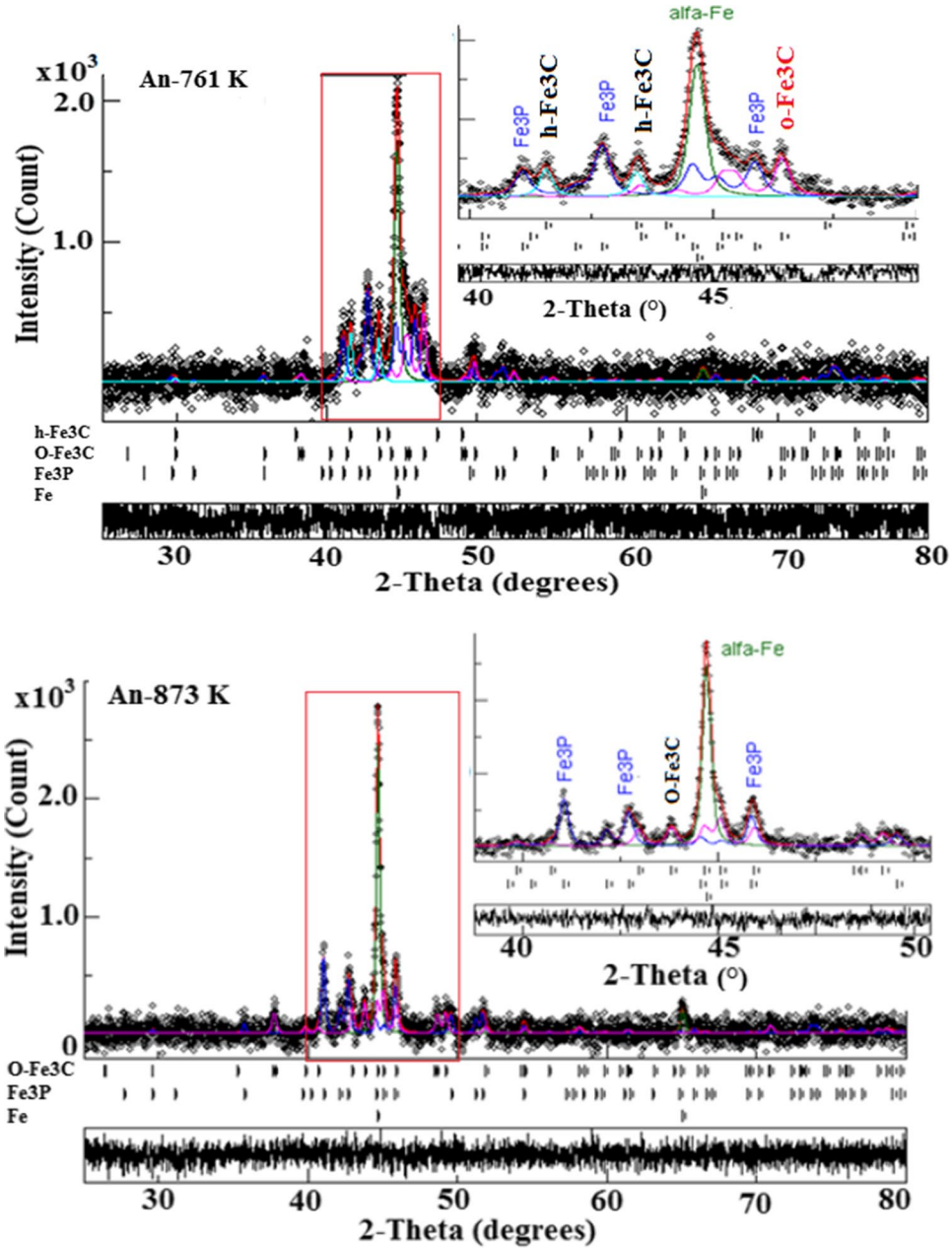

Fig. 3 Typical Rietveld refinement of the XRD patterns of the annealed ribbons at 761 K ($R_{wp}=1.46\%$, $R_{exp}=1.35\%$, $R_b=1.15\%$, Sig = 1.07), and 873 K (Sig = 0.99, $R_{wp}=1.59\%$, $R_{exp}=1.59\%$, $R_b=1.26\%$)

Table 2 Lattice parameters, relative deviations, and weight fractions of the different phases obtained at different annealing temperatures

T(K)	Phase	a (nm) $\pm 10^{-4}$	$\Delta a/a$	b (nm) $\pm 10^{-4}$	$\Delta b/b$	c (nm) $\pm 10^{-4}$	$\Delta c/c$	Weight fraction %
729	α-Fe	0.2865	–0.034	–	–	–	–	09.2
	Amorphous	–	–	–	–	–	–	90.8
	α-Fe	0.2865	−0.024	–	–	–	–	25.3
	Fe_3P	0.9081	−0.26	–	–	0.4479	0.318	44.6
761	θ-Fe_3C	0.5011	−1.362	0.6675	–1.213	0.4476	−0.909	20.8
	ε-Fe_3C	0.4744	−0.474	–-	–	0.4341	−0.284	09.3
	α-Fe	0.2864	−0.059	–	–	–	–	28.80
873	Fe_3P	0.9087	−0.199	–	–	0.4480	0.356	38.20
	θ-Fe_3C	0.5079	−0.017	0.6735	–0.327	0.4521	0.081	33.00

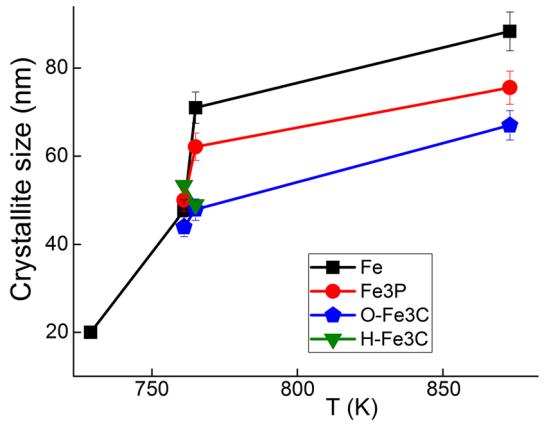

Fig. 4 Evolution of the average crystallite size of the different phases as a function of the annealing temperature.

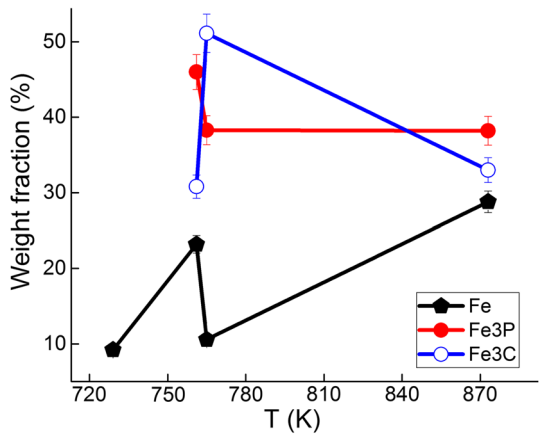

Fig. 5 Variation of the weight fractions of α-Fe-type, Fe_3P-type and Fe_3C-type phases as a function of the annealing temperature

Fe_3C-type and Fe_3P-type phases may be attributed to the off-stoichiometry of the phosphide and carbide compounds, and/or defects such as vacancies and interstitials. In the case of cementite, since carbon atoms are located in interstitial sites, any deficit from the 3:1 for the Fe:C atom ratio is generally related to interstitial vacancies as inferred from lattice parameter contraction and change in the volume of the unit cell. Besides, the formation of carbon vacancies in, or carbon stuffing into, Fe_3C produces non-stoichiometry, disturbs and weakens the iron magnetic ordering.

The occurrence of the crystallization/nanocrystallization within the amorphous matrix and the type of atomic diffusion on annealing can be followed by the apparent activation energy (E_a). This latter represents the minimum energy that is required to activate atoms to overcome the energy barrier of the nucleation and to reach the transition state. The activation energy can be evaluated from the variation of the crystallization temperature as a function of the heating rate by using the Kissinger method of thermally stimulated processes [55]. This method is based on the shift of the exothermic peak temperature (T_p) as a function of the heating rate according to the following relation [55]:

$$\ln\left(\frac{\beta}{T_p^2}\right) = -\frac{E_a}{RT_p} + \text{const}, \tag{2}$$

where E_a is the apparent activation energy, $R = 8.314\,\text{J.mol.}^{-1}K^{-1}$ is the gas constant, and β is the heating rate. The plot of $\ln\left(\frac{\beta}{T_p^2}\right)$ versus $1/T_p$ (Fig. 6) is a straight line, and the apparent activation energy for crystallization can be calculated from its slope. The value of E_a decreases from 499.5 kJ/mol for the first stage to 368.9 kJ/mol for the third stage. The higher E_a value (499.5 ± 6 kJ/mol) at the beginning of the nanocrystallization indicates that the precipitation of the first nanocrystallites requires more energy to overcome the crystallization barrier and form nuclei, while its decrease is due to the existence of NC nucleus/phases. Indeed, activation energy value includes the energy used for nucleation and growth. The higher activation energy value (499.5 kJ/mol) for the first stage means that the time required to crystallize 9% of the alloy at 729 K may exceeds million years, when the amorphous alloys is added to concrete to reinforce it. A comparable value of E_a was reported for the amorphous $Fe_{80}P_9B_2C_9$ alloy ($E_a = 496$ kJ/mol) [35], while different values were obtained for the $Fe_{77}Cr_4P_8C_{11}$ ($E_a = 209$ kJ/mol) [56] and $Fe_{80}P_{13}C_7$ ($E_a = 298$ kJ/mol) amorphous ribbons [57].

Figure 7 shows the morphology of the melt-spun ribbons. The free side exhibits a smooth surface without obvious defects, while the wheel side shows some defects such as pores and cracks. The microstructure of the annealed ribbons at 873 K consists of lamella, fine platelets, alternate planes of ferrite and cementite, and grains

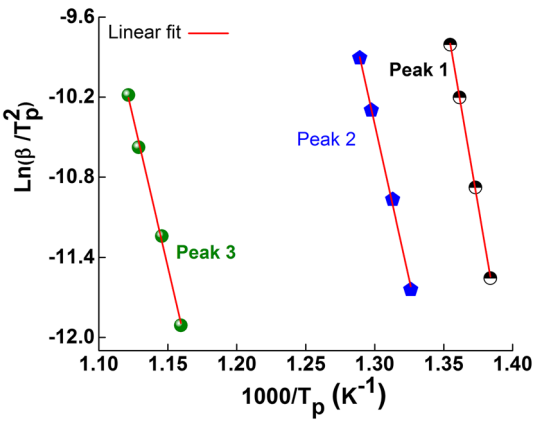

Fig. 6 ln (β/T^2) plot against $1000/T_p$. The activation energy is determined from the slope of the straight line

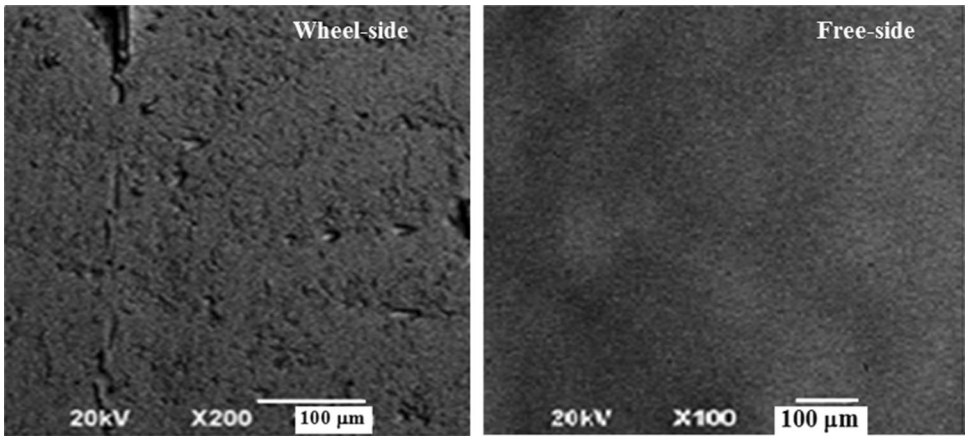

Fig. 7 SEM micrographs of the melt-spun ribbons

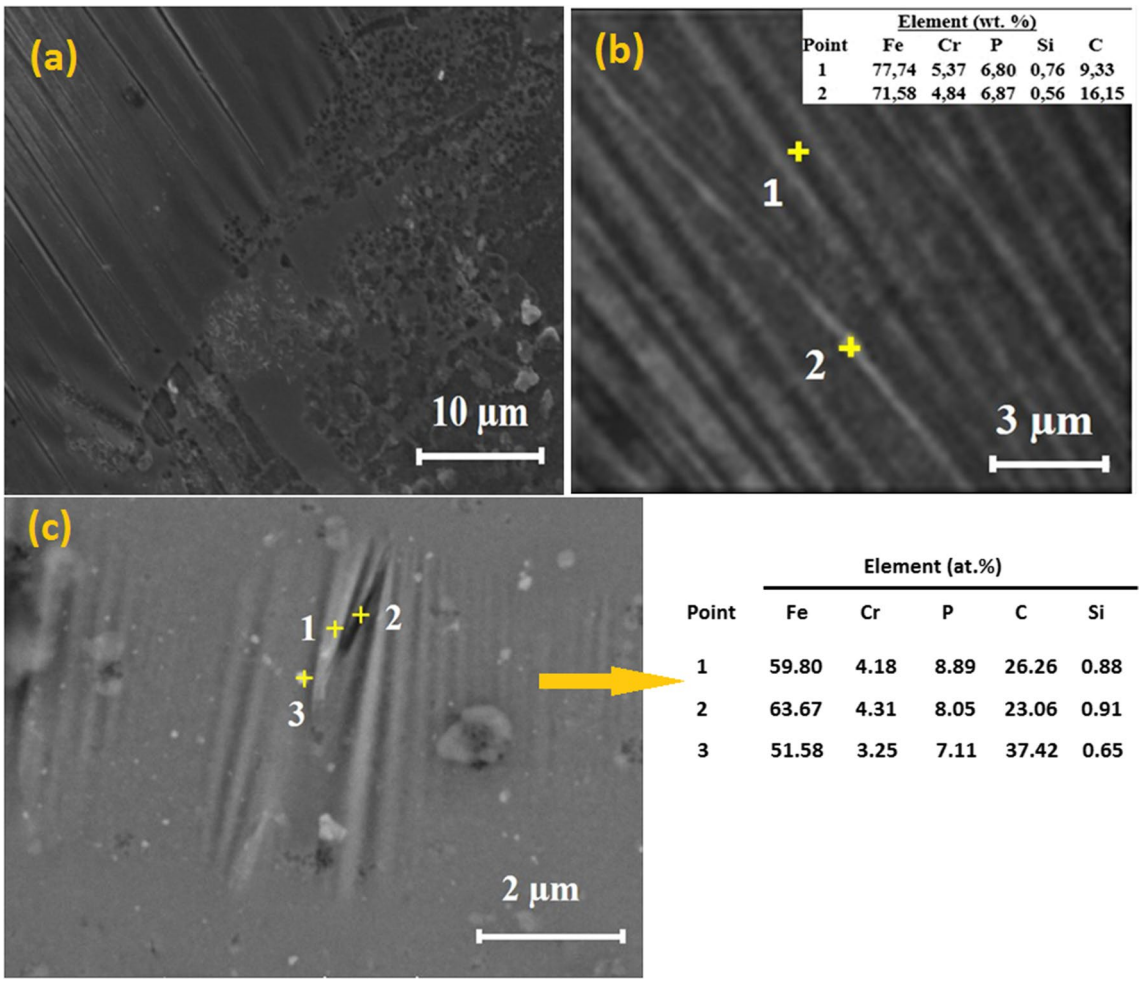

Fig. 8 **a** Typical SEM image microstructure of the annealed ribbons at 873 K obtained using secondary electron detector. **b** Image of the lamellar pearlite area shown in the up of obvious image, obtained by backscattered electrons. **c** Backscattered electrons image of another lamellar pearlite zone in transformation

with different shapes and sizes (Fig. 8). In general, ferrite grains preferentially precipitate on lattice defects in cementite and grow in the form of parallel lamella separated by carbide lamella forming lamellar pearlite. According to their elemental composition, the dark lamella belongs to ferrite ($Fe_{77.74}P_{6.89}Cr_{5.37}C_{9.33}Si_{0.67}$), and the carbon-rich

($Fe_{71.58}P_{6.87}Cr_{4.84}C_{16.15}Si_{0.56}$) clear lamella belongs to Fe_3C carbide (Fig. 8b). Another lamellar pearlite area on formation at the same annealing temperature (873 K) is shown in Fig. 8c. The elemental analyses of different points related to clear lamella (point 1), dark lamella (point 2), and fine precipitate reveal that at this stage of treatment, the transformation is not complete as mentioned above in DSC results. The transformation occurs heterogeneously depending on the amorphous ribbons' local chemical composition throughout the temperature range between the onset (T_x) and endset (T_e) temperatures. The fine precipitate (point 3) contains less iron and chromium but more carbon than the lamellae. Furthermore, the heterogeneity of the microstructure is evidenced by the presence of different morphologies related to the formation of carbide, phosphide, and solid solutions. The elemental analysis confirms the presence of all elements, as shown in Table 3. One notes that Fe content fluctuates between 17.46 and 75.13 wt.%, Cr content fluctuates between 1.73 and 6.77 wt.%, P content varies between 2.77 and 11.45 wt.%, and C content varies between 8.75 and 78 wt.% (see Fig. 9). Despite the variations in compositions locally from one point to another, the elemental mapping shows that the distribution of Fe, Cr, and P elements is nearly uniform (Fig. 10a), while that of C is less homogeneous. Such distribution is also confirmed by the concentration profile where C content shows small fluctuations (Fig. 10b). Those observations agree well with the fact that chromium forms SS with iron, and phosphorous easily combines with iron forming a Fe-Fe_3P type eutectic. At the same time ferrite has a shallow carbon solubility limit (< 0.02%). The variations in composition are related to the presence of different phases during the crystallization process, as shown above by XRD results. Likewise, the homogeneous distribution of Fe, Cr, P, and C elements in the amorphous matrix reveals the absence of the elements segregation, which can be nonuseful for the mechanical properties.

Table 3 EDX analysis related to the spot locations marked as 1–11 in the SEM image shown in Fig. 13

Point	Element (wt. %)			
	Fe	Cr	P	C
1	68.93	6.55	11.45	13.07
2	67.18	6.12	11.20	15.50
3	75.44	5.45	9.56	9.55
4	17.46	1.73	2.77	78.04
5	32.62	3.14	4.86	59.38
6	70.08	6.11	10.39	13.42
7	73.90	5.57	9.26	11.27
8	75.13	5.73	9.67	9.47
9	73.40	6.71	11.14	8.75
10	72.33	6.77	10.91	9.99
11	72.47	5.50	8.78	13.25

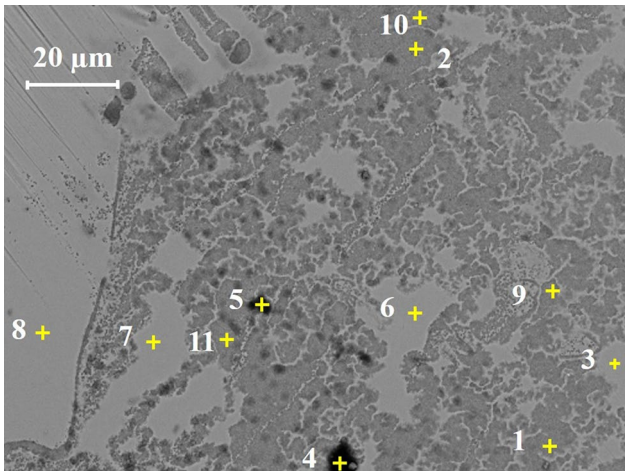

Fig. 9 Typical SEM image of the annealed ribbons showing the microstructural heterogeneity

3.2 Magnetic properties

The hysteresis loops of the melt-spun ribbons show different behaviors depending on whether the magnetic field is applied in the plane or out of the plane of the ribbons (Fig. 11). For the former, the ribbons exhibit typical soft magnetic hysteresis loop with a rectangular shape characteristic of an axial anisotropy, whereas for the later the hysteresis loop does not saturate which means that the axis of easy magnetization is in the plane of the ribbons. The annealed samples show rectangular hysteresis loops with small losses and a reduction in the magnetization up to 758 K, but exhibit sigmoidal shapes and an increase in the saturation magnetization (M_s) as the annealing temperature increases to 775 and 933 K (Fig. 12). The inset shows the enlargement of the low magnetic field region. The alloy composition, particle morphology, particle size, crystal structure, magnetic anisotropy, and crystallite size can influence the magnetic properties.

The coercivity (H_c) increases slightly with increasing temperature from 16.59 Oe for the amorphous ribbons to approximately 19.77 Oe at 758 K, increases to a maximum value of approximately 218.34 Oe at 775 K, and then decreases to 172.79 Oe at 933 K (Table 4). The increase in the coercivity may be related to the grain growth, atomic ordering, and the presence of non-magnetic precipitates that hinder the movement of the Bloch walls. The saturation magnetization (Ms) can be affected by the crystal structure, the local environment of the magnetic iron atoms and the exchange of magnetic Fe–Fe, Fe–Cr, Fe–P, and Fe–C interactions at the nearest-neighbor shell. The decrease in Ms at 758 K can be ascribed to the variation in the local

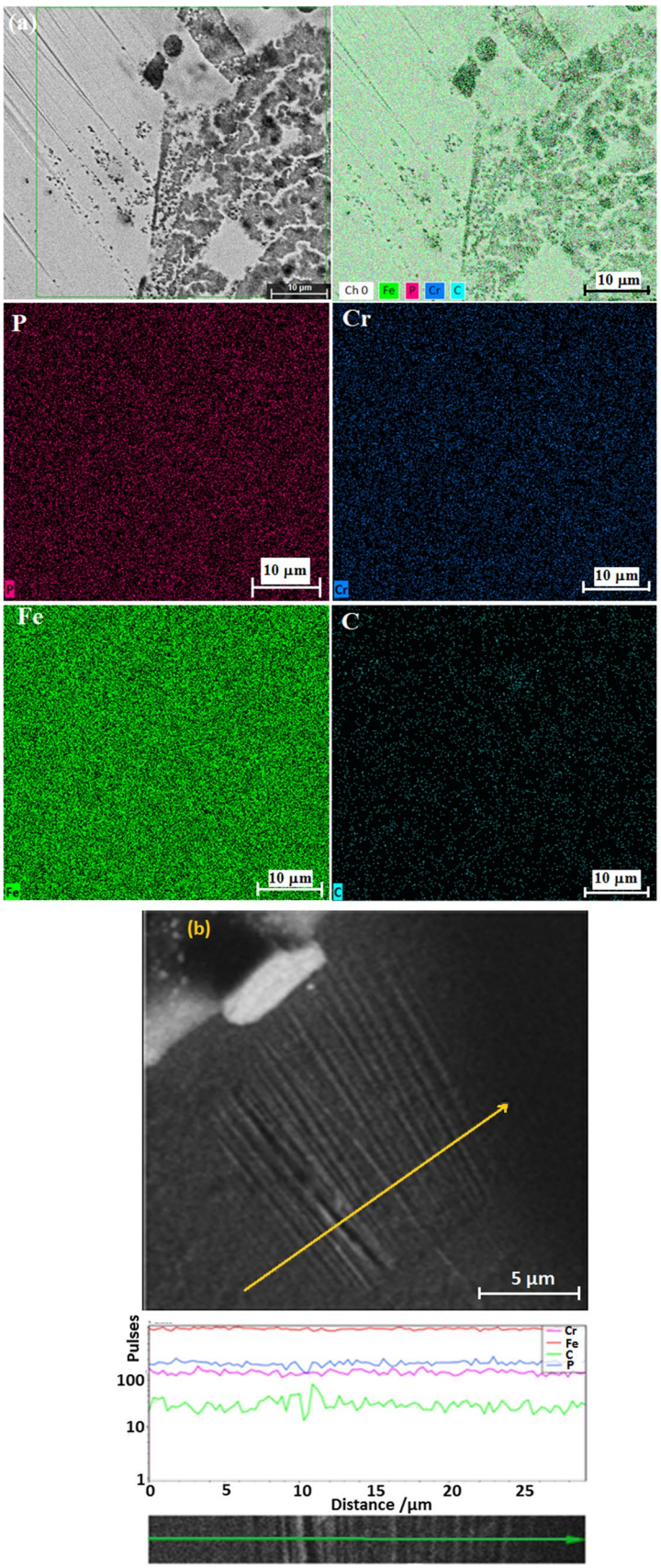

Fig. 10 EDX elemental mapping for the annealed ribbons at 873 K (**a**); and elemental line scan along the indicated line (**b**)

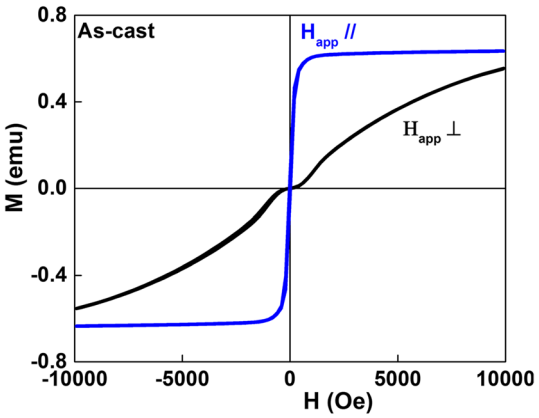

Fig. 11 Hysteresis loops of the melt-spun ribbons under an applied magnetic field in the ribbons plane (H_{app} //) and out of the ribbons plane (H_{app} ⊥)

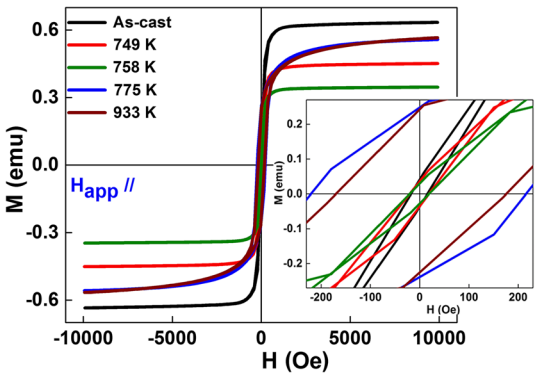

Fig. 12 Hysteresis cycles of the annealed ribbons at different temperatures with that of the as-cast ribbons for comparison. The inset shows the enlargement of the central part.

Table 4 Variation of the coercivity (H_c), saturation magnetization (M_s), remanance (M_r), and squareness M_r/M_s ratio as a function of the annealing temperature

Sample	Magnetic properties			
	H_c (Oe)	M_r (emu)	M_s (emu)	M_r/Ms
Melt-spun	16.59	0.038	0.635	0.061
An-749 K	19.61	0.036	0.451	0.079
An-758 K	19.77	0.028	0.346	0.082
An-783 K	218.34	0.244	0.558	0.436
An-933 K	172.79	0.234	0.566	0.413

Fe environment through the diffusion of Cr, C, and P elements into the Fe matrix. Indeed, the metalloid P and C elements contribute electrons to the unfilled *d*-band of the Fe atom and decrease the moment per metal atom. Likewise, the presence of Cr causes a rapid drop in the Fe moment since the moments of Cr atoms align anti-ferromagnetically with the dominant Fe moments. This observation agrees well with the XRD results since the minimum of Ms corresponds to a maximum weight fraction of Fe_3C-type and Fe_3P-type phases (89.4%). Additionally, the slight improvement in saturation magnetization above 773 K may be correlated to the atomic ordering and the increase in the α-Fe-type solid solution weight fraction to about 28.8% (Fig. 5). Furthermore, the variation of *Ms* may be linked to the lattice parameter value which is related to the interatomic distance. Likewise, the ferromagnetic exchange interaction between adjacent magnetic moments depends on the interatomic distances. Thus, the density of states at the Fermi level changes with the lattice parameter change leading to an indirect effect on *Ms*. The variation of the remanence (M_r) exhibits the same tendency as that of *Ms*. In line with the squareness ratio values, amorphous and annealed ribbons at 749 K and 758 K are multidomain ($M_r/M_s < 0.1$), while those annealed at 775 and 933 K are pseudo-single domains [58] with M_r/M_s of approximately 0.43 and 0.41, respectively.

Figure 13 displays the temperature dependence of magnetization of amorphous and annealed ribbons. The first derivative d*M*/d*T* curves are shown in the inset. For the amorphous ribbons, the magnetization decreases gradually with the increasing temperature up to 623 K and drops to zero, indicating that the Curie temperature of the amorphous phase was reached. The increase in the magnetization, in two distinct steps, as the temperature increases and approaches the crystallization temperature above 673 K can be linked to the formation of new magnetic phases. The value of $T_C = 447.4$ K corresponds to the minimum in the *dM/dT* curve, while the crystallization temperatures of about 738 K and 838.84 K match the maximum of d*M*/d*T* curve. The magnetization curves shift to higher temperatures for the annealed ribbons as the crystalline fraction transformed increases and drops to zero at T_C. The presence of different T_C values for the annealed ribbons at 749 K, might be attributed to the residual amorphous phase ($T_C = 406$ K) and the formation of Fe_3C carbide ($T_C = 488$ K). Similar behavior has been reported for the $Fe_{52}Co_{10}Nb_8B_{30}$ amorphous ribbons where the Curie temperature shifted to higher temperatures with increasing the crystalline fraction transformed [59]. According to the alloy composition and preparation conditions, different Curie temperatures have been reported for the cementite in the literature [60–63]. The influence of each atomic species on the exchange interaction can be affected by the contents of Cr, P, and C. The Curie temperature of the annealed ribbons at 775 K and 933 K increases to approximately 593 K and 638 K, respectively. The lower values of T_C compared to those of pure α-Fe (1033 K) and Fe_3P (723 K [64], 686 K [65], and 716 K [60]) indicate that the presence of non-magnetic atoms in the vicinity of Fe ones modifies the nearest-neighbor coordinates. Likewise,

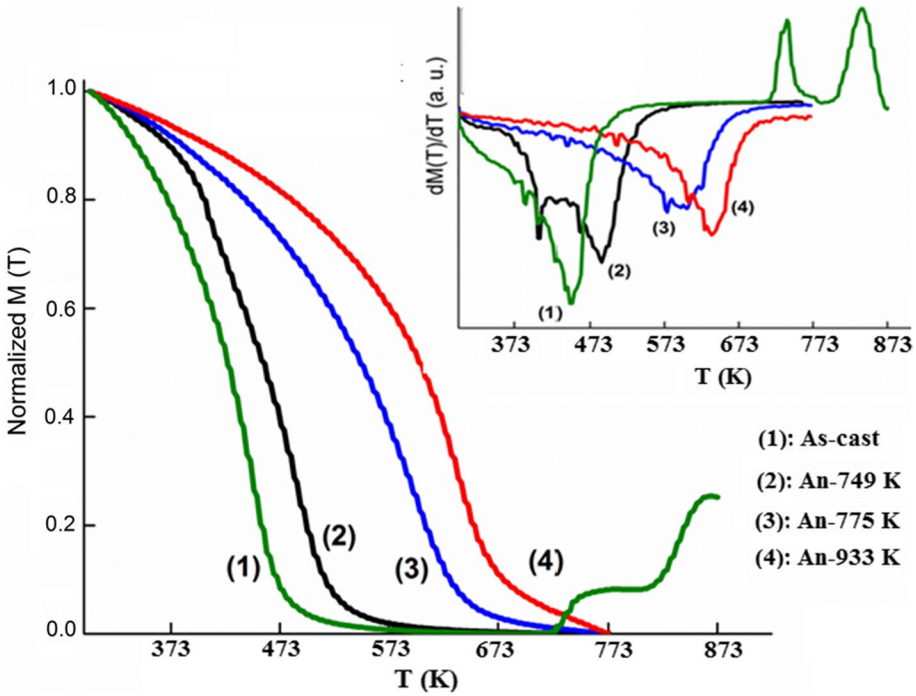

Fig. 13 Temperature dependence of magnetization for melt-spun and annealed ribbons. The first derivative d*M*/d*T* of magnetization is shown in the inset

T_C is proportional to the exchange-integral constant, A, which is influenced by the type of alloying element and the distance between magnetic elements. The exchange-integral constant A is correlated to Fe–Fe interaction for the Fe–Cr–P–C amorphous ribbons since there is only one magnetic element. Furthermore, the addition of metalloid elements such as C and P increases the distance between two Fe atoms leading to an increase in the Curie temperature of the annealed ribbons.

4 Conclusions

The crystallization process in the melt-spun $Fe_{86}Cr_6P_6C_2$ ribbons was investigated by XRD, SEM, DSC, and VSM. The main results are as follows:

- The DSC curves reveal the presence of three crystallization stages in the temperature range of 673–973 K. The XRD results show a composite structure where NC α-Fe crystals are embedded into the amorphous matrix for the annealed ribbons at 729 K and a mixture of α-Fe-, Fe_3P, and θ-Fe_3C at 933 K.
- The crystallite size increases with increasing annealing temperature and remains at the nanometer scale (20–88 nm).
- The microstructure of the annealed ribbons consists of lamella, fine platelets, alternate planes of ferrite and cementite, and grains with different shapes and sizes.
- The Curie temperature of the amorphous phase is about $T_C = 475$ K. T_C increases with increasing temperature from 447.4 K for the melt-spun ribbons to 638 K at 933 K.
- The melt-spun ribbons exhibit a low coercivity of 16.598 Oe and a high saturation magnetization of 0.635 emu compared to the annealed ones.
- The annealed ribbons are multidomain up to 758 K ($M_r/M_s < 0.1$) and pseudo-single domain above 773 K ($M_r/M_s \sim 0.43$).
- The apparent activation energy drops from 499 kJ/mol for the first crystallization stage to 369 kJ/mol for the third crystallization stage.
- The ribbons remain at the nanometer scale even after annealing at 933 K with good magnetic properties.

Acknowledgements Special mention to the late Prof. M. Zergoug from the Industrial Techniques Research Center. We would like to thank Mr Foued Khammaci from LM2S Laboratory for the XRD and VSM measurements. L. Abadlia would like to thank Prof. J.-G. Gasser from the University of Lorraine (France) for his constant help.

Data availability The datasets generated during and/or analyzed during the current study are available from the corresponding author on reasonable request.

Declarations

Conflict of interest The authors declare that they have no conflict of interest.

References

1. A. Kupczyk, J. Świerczek, M. Hasiak, K. Prusik, J. Zbroszczyk, P. Gębara, Microstructure and some thermomagnetic properties of amorphous Fe-(Co)-Mn-Mo-B alloys. J. Alloys Compd. **735**, 253–260 (2018). https://doi.org/10.1016/j.jallcom.2017.10.278
2. C. Souza, D. Ribeiro, C. Kiminami, Corrosion resistance of Fe-Cr-based amorphous alloys: an overview. J. Non-Cryst. Solids **442**, 56 (2016). https://doi.org/10.1016/j.jnoncrysol.2016.04.009
3. G. Zhang, H. Zhang, S. Yue, A. Wang, A. He, R. Cheng, C.T. Liu, Ultra-low cost and energy-efficient production of FePCSi amorphous alloys with pretreated molten iron from a blast furnace. J. Non-Cryst. Solids **514**, 108–115 (2019). https://doi.org/10.1016/j.jnoncrysol.2019.03.045
4. Y. Fan, S. Zhang, X. Xu, W. Miao, J. Zhang, T. Wang, C. Chen, R. Wei, F. Li, Effect of the substitution of Si for B on thermal stability, magnetic properties and corrosion resistance in novel Fe-rich amorphous soft magnetic alloy. Intermetallics **138**, 107306 (2021). https://doi.org/10.1016/j.intermet.2021.107306
5. A. Wang, C. Zhao, H. Men, A. He, C. Chang, X. Wang, R.W. Li, Fe-based amorphous alloys for wide ribbon production with high Bs and outstanding amorphous forming ability. J. Alloy Compd. (2015). https://doi.org/10.1016/j.jallcom.2015.01.056
6. T. Bitoh, D. Watanabe, Effect of yttrium addition on glass-forming ability and magnetic properties of Fe–Co–B–Si–Nb bulk metallic glass. Metals **5**, 1127–1135 (2015). https://doi.org/10.3390/met5031127
7. M. Shi, Z. Liu, T. Zhang, Effects of minor Sn addition on the glass formation and properties of Fe- metalloid metallic glasses with high magnetization and high glass forming ability. J. Magn. Mater. **378**, 417–423 (2015). https://doi.org/10.1016/j.jmmm.2014.10.144
8. G.Y. Koga, C. Bolfarini, C.S. Kiminami, A.M. Jorge, W.J. Botta, An overview of thermally sprayed Fe-Cr-Nb-B metallic glass coatings: from the alloy development to the coating's performance against corrosion and wear. J. Therm Spray Tech. **31**(4), 923–955 (2022). https://doi.org/10.1007/s11666-022-01371-7
9. A. Łukiewska, P. Gębara, Structure, magnetocaloric effect and critical behavior of the $Fe_{60}Co_{12}Gd_4Mo_3B_{21}$ amorphous ribbons. Materials **15**(1), 34 (2021). https://doi.org/10.3390/ma15010034
10. L. Pei, X. Zhang, Z. Yuan, Application of Fe-based amorphous alloy in industrial wastewater treatment: a review. J. Renew. Mater. **10**(4), 969 (2022). https://doi.org/10.32604/jrm.2022.017617
11. Y. Takahara, K. Hatade, H. Matsuda, Reversible structural relaxation in $Fe_{78}B_7Si_{15}$ and $Fe_{40}Ni_{40}P_{14}B_6$ amorphous alloys. Trans. Jap. Inst. Metals **29**(10), 774–780 (1988). https://doi.org/10.2320/matertrans1960.29.774
12. T. Egami, Structural relaxation in amorphous alloys-compositional short range ordering. Mater. Res. Bull. **13**, 557–562 (1978). https://doi.org/10.1016/0025-5408(78)90178-2
13. F.C. Li, T. Liu, J.Y. Zhang, S. Shuang, Q. Wang, A.D. Wang, Y. Yang, Amorphous– nanocrystalline alloys: fabrication, properties, and applications. Mat. Today Adv. **4**, 100027 (2019). https://doi.org/10.1016/j.mtadv.2019.100027
14. A. Cotai, S. Miraglia, B. Neamţu, T. Marinca, H. Chicinaş, O. Isnard, I. Chicinaş, A comparative study of nanocrystalline $Fe_{38.5}Co_{38.5}$ Nb_7 $P_{15}Cu_1$ alloys obtained by mechanical alloying and rapid quenching. Arch. Metal. Mater. **67**(2), 555–561 (2022). https://doi.org/10.24425/amm.2022.137790
15. J.A. Moya, S.G. Caramella, C. Berejnoi, Evolution of soft magnetic, mechanical and electrical properties measured simultaneously during annealing of rapidly solidified alloys. J. Magn. Magn. Mat. **476**, 248–253 (2019). https://doi.org/10.1016/j.jmmm.2019.01.008
16. L.L. Pang, A. Inoue, E.N. Zanaeva, F. Wang, A.I. Bazlov, Y. Han, F.L. Kong, S.L. Zhu, R.B. Shull, Nanocrystallization, good soft magnetic properties and ultrahigh mechanical strength for Fe82- 85B1316Si1Cu1 amorphous alloys. J. Alloys Compd. **785**, 25–37 (2019). https://doi.org/10.1016/j.jallcom.2019.01.150
17. P. Gębara, M. Hasiak, Investigation of critical behavior in the vicinity of ferromagnetic to paramagnetic phase transition in the $Fe_{75}Mo_8Cu_1B_{16}$ alloy. J. Appl. Phys. **124**, 083904 (2018). https://doi.org/10.1063/1.5039509
18. A. Łukiewska, J. Olszewski, M. Hasiak, P. Gębara, Magnetocaloric effect in amorphous and partially crystallized $Fe_{80}Zr_7Cr_6Nb_2Cu_1B_4$ alloy. Acta Phys. Pol A **133**(3), 676–679 (2018). https://doi.org/10.12693/APhysPolA.133.676
19. R. Babilas, A. Radoń, P. Gębara, Structure and magnetic properties of Fe-B-Si-Zr metallic glasses. Acta Phys. Pol A **131**(4), 726–728 (2017). https://doi.org/10.12693/APhysPolA.131.726
20. J. Zhou, J. You, K. Qiu, Advances in Fe-based amorphous/nanocrystalline alloys. J. Appl. Phys. **132**(4), 040702 (2022). https://doi.org/10.1063/5.0092662
21. J. Xu, Y. Yang, Q. Yan, C. Fan, F. Hou, Z. Xie, Effect of micro-alloying on crystallization behavior, magnetic properties and bending ductility of high Fe content FeSiBCuPC alloys. J. Alloys Compd. **777**, 499–505 (2019). https://doi.org/10.1016/j.jallcom.2018.11.029
22. C. Suryanarayana, A. Inoue, *Bulk metallic glasses* (CRC Press, 2017). https://doi.org/10.1201/9781315153483
23. N. Bensebaa, S. Alleg, F.Z. Bentayeb, L. Bessais, J.M. Greneche, Microstructural characterization of Fe–Cr–P–C powder mixture prepared by ball milling. J. Alloys Compd. **388**(1), 41–48 (2005). https://doi.org/10.1016/j.jallcom.2004.06.075
24. B. Huang, C. Zhang, G. Zhang, H. Liao, Wear and corrosion resistant performance of thermal- sprayed Fe-based amorphous coatings: a review. Surf. Coat. Technol. **377**(4), 124896 (2019). https://doi.org/10.1016/j.surfcoat.2019.124896
25. B. Bouzabata, S. Alleg, Products of crystallization of amorphous alloy of $Fe_{77}Cr_4P_8C_{11}$ and sequences of precipitation. J. Alloys Compd. **178**(1–2), 117–124 (1992). https://doi.org/10.1016/0925-8388(92)90252-5
26. P. Hua, B. Wang, C. Yu, Y. Han, Q. Sun, Shear-induced amorphization in nanocrystalline NiTi micropillars under large plastic deformation. Acta Mater. **241**, 118358 (2022). https://doi.org/10.1016/j.actamat.2022.118358
27. X. Yu, J. Wang, L. Wang, W. Huang, Fabrication and characterization of CrNbSiTiZr high-entropy alloy films by radio-frequency magnetron sputtering via tuning substrate bias. Surf. Coat. Technol. **412**, 127074 (2021). https://doi.org/10.1016/j.surfcoat.2021.127074
28. M. Nabiałek, Fabrication methods for bulk amorphous alloys, in *Alloy Materials and Their Allied Applications*. ed. by I. Inamuddin, R. Boddula, M.I. Ahamed, A.M. Asiri (Wiley Online Library, 2020), pp.1–26. https://doi.org/10.1002/9781119654919.ch1
29. J. Zhao, Q. Gao, H. Wang, F. Shu, H. Zhao, W. He, Z. Yu, Microstructure and mechanical properties of Co-based alloy coatings fabricated by laser cladding and plasma arc spray welding. J. Alloys Compd. **785**, 846–854 (2019). https://doi.org/10.1016/j.jallcom.2019.01.056
30. Q. Yan, Y. Gao, C. Du, Z. Yao, Y. Mo, Ultrasonic-assisted shearing characteristics of Fe-based amorphous alloy strips. J. Mater. Eng. Perf. (2022). https://doi.org/10.1007/s11665-022-06952-9
31. D.H. Milanez, L.I.L. Faria, D.R. Leiva, C.S. Kiminami, W.J. Botta, Assessing technological developments in amorphous/glassy metallic alloys using patent indicators. J. Alloys Compd. **716**, 330–335 (2017). https://doi.org/10.1016/j.jallcom.2017.05.105

32. N.K. Maroju, X. Jin, Mechanism of chip segmentation in orthogonal cutting of Zr-based bulk metallic glass. J. Manuf. Sci. Eng. **141**, 081003 (2019). https://doi.org/10.1115/1.4043837
33. H.P. Tsui, P.H. Lee, C.C. Yeh, J.C. Hung, Ultrasonic vibration-assisted electrical discharge machining on Fe-based metallic glass by adding conductive powder. Proc. CIRP **95**, 425–430 (2020). https://doi.org/10.1016/j.procir.2020.02.275
34. B. De Guillebon, M. Henry, G. Le Gal, C. Tete, Mechanical and magnetic properties of amorphous FeCrPC ribbons and wires. Mat. Sci. Eng. **98**, 539–542 (1988). https://doi.org/10.1016/0025-5416(88)90225-X
35. J. Wang, Y. Di, Z. Fang, S. Guan, T.J. Zhang, Thermal stability, crystallization and soft magnetic properties of Fe-P-C-based glassy alloys. Non-Cryst. Solids **454**, 39–45 (2016). https://doi.org/10.1016/j.jnoncrysol.2016.10.014
36. G. Le Gal, M. Henry, F. Varret, Effect of elaboration velocity on magnetic properties of melt spun amorphous metal ribbons. Revue Phys. App. **22**(8), 729–734 (1987). https://doi.org/10.1051/rphysap:01987002208072900
37. K. Asami, K. Hashimoto, T. Masumoto, S. Shimodaira, ESCA study of the passive film on an extremely corrosion-resistant amorphous iron alloy. Corr. Sci. **16**(12), 909–914 (1976). https://doi.org/10.1016/S0010-938X(76)80010-8
38. I. Raya, S. Chupradit, M.M. Kadhim, M.Z. Mahmoud, A.T. Jalil, A. Surendar, A.N. Bochvar, Role of compositional changes on thermal, magnetic, and mechanical properties of Fe-PC-based amorphous alloys. Chin. Phys. B **31**(1), 016401 (2022). https://doi.org/10.1088/1674-1056/ac3655
39. T. Shmyreva, J. Knapp, Nano-amorphous coatings for medical instruments. In: Medical Device Materials: Proceeding Materials and Processes for Medical Devices Conference., 103–107 (2004)
40. J.M. Boucheret, Concrete and mortars reinforced with FIBRAFLEX amorphous metallic fibers. In: Workshop on fiber reinforced cement and concrete. University of Sheffield, Sheffield (2004).
41. J.M. Boucheret, 18 wet sprayed mortars reinforced with flexible metallic fibres for renovation: basic requirements and full-scale experimentation. Sprayed Concr. Technol. **2**, 166 (2002)
42. M. Bourrous, F. Varret, Activation energy distribution in amorphous Fe-Cr–PC alloy, determined for Tc measurements during structural relaxation. Solid state Comm. **57**(8), 713–716 (1986). https://doi.org/10.1016/0038-1098(86)90358-3
43. https://www.saint-gobain-seva.com/fr
44. L. Lutterotti, MAUD version 2.992, http://maud.radiographema.com/. Accessed 28 Nov 2023
45. H.M. Rietveld, The Rietveld method. Phys. Scr. **89**(9), 098002 (2014). https://doi.org/10.1088/0031-8949/89/9/098002
46. T. Paul, A. Loganathan, A. Agarwal, S.P. Harimkar, Kinetics of isochronal crystallization in a Fe-based amorphous alloy. J. Alloys Compd. **753**, 679–687 (2018). https://doi.org/10.1016/j.jallcom.2018.04.133
47. Y. Wang, X. Li, L. Yue, G. Yang, Z. Li, Q. Sun, M. Xu, J. Yi, Crystallization sequence of an (Al86Ni9La5)98Si2 amorphous alloy under continuous heating. J. Non-Cryst. Solids **610**, 122310 (2023). https://doi.org/10.1016/j.jnoncrysol.2023.122310
48. P. Wang, M. Wei, Y. Dong, Z. Zhu, J. Liu, J. Pang, J. Zhang, Crystallization evolution behavior of amorphous $Fe_{85.7}Si_{7.9}B_{3.6}Cr_2C_{0.8}$ powder produced by a novel atomization process. J. Non- Cryst. Solids **594**, 121824 (2022). https://doi.org/10.1016/j.jnoncrysol.2023.122373
49. A.H. Cai, G. Zhou, P.W. Li, D.W. Ding, Q. An, G.J. Zhou, H. Mao, Crystallization kinetics of $Cu_{50}Zr_{40}Ti_{10}$ amorphous powder. Thermochim. Acta **714**, 179261 (2022). https://doi.org/10.1016/j.tca.2022.179261
50. D. Janovszky, M. Sveda, A. Sycheva, F. Kristaly, F. Zámborszky, T. Koziel, P. Bala, G. Czel, G. Kaptay, J. Term. Anal. Calorim. **147**, 7141–7157 (2022). https://doi.org/10.1007/s10973-021-11054-0
51. S. Nagakura, Study of metallic carbides by electron diffraction Part III. Iron carbides. J. Phys. Soc. Jpn. **14**, 186–195 (1959). https://doi.org/10.1143/JPSJ.14.186
52. P. Rezaei-Shahreza, A. Seifoddini, S. Hasani, Thermal stability and crystallization process in a Fe-based bulk amorphous alloy: the kinetic analysis. J. Non-Cryst. Solids **471**, 286–294 (2017). https://doi.org/10.1016/j.jnoncrysol.2017.05.044
53. H. Göhring, A. Leineweber, E.J. Mittemeijer, A thermodynamic model for non-stoichiometric cementite; the Fe–C phase diagram. Calphad **52**, 38–46 (2016). https://doi.org/10.1016/j.calphad.2015.10.014
54. H.K.D.H. Bhadeshia, Cementite. Int. Mat. Rev. **65–1**, 1–27 (2020). https://doi.org/10.1080/09506608.2018.1560984
55. H.E. Kissinger, Variation of peak temperature with heating rate in differential thermal analysis. J. Res. Natl. Bur. Stand. **57**, 217–221 (1956). https://doi.org/10.1021/ac60131a045
56. B. Bouzabata, S. Alleg, Kinetics of crystallization of the amorphous alloy $Fe_{77}Cr_4P_8C_{11}$. Mat. Chem. Phys. **33**(1–2), 70–75 (1993). https://doi.org/10.1016/0254-0584(93)90092-Z
57. F. Sun, T. Gloriant, Primary crystallization process of amorphous $Al_{88}Ni_6Sm_6$ alloy investigated by differential scanning calorimetry and by electrical resistivity. J. Alloys Compd. **477**, 133–138 (2009). https://doi.org/10.1016/j.jallcom.2008.10.021
58. S. Alleg, L. Hamza, M. Ibrir, S. Souilah, W. Tebib, N.E. Fenineche, J.M. Greneche, Microstructural, hyperfine and magnetic properties FeSiBCuNb deposits. J. Supercond. Nov Magn **28**(4), 2431–2439 (2015). https://doi.org/10.1007/s10948-015-3038-1
59. T. Gloriant, S. Surinach, M.D. Baró, Stability and crystallization of Fe–Co–Nb–B amorphous alloys. J. Non-Cryst. Solids **333**(3), 320–326 (2004). https://doi.org/10.1016/j.jnoncrysol.2003.10.007
60. A.J.P. Meyer, M.C. Cadeville, Magnetic properties of iron-phosphorus compounds. J. Phys. Soc. Jpn. **17**, 223–225 (1962)
61. M. Acet, H. Herper, P. Entel, E.F. Wassermann, The phase stability of ε-Fe alloys. J. Phys. IV **11**(PR8), 229–234 (2001). https://doi.org/10.1051/jp4:2001839
62. A. Tsuzuki, S. Sago, S.I. Hirano, High-temperature and pressure preparation and properties of iron carbides Fe_7C_3 and Fe_3C. J. Mater. Sci. **19**, 2513–2518 (1984). https://doi.org/10.1007/BF00550805
63. I.G. Wood, L. Vocadlo, K.S. Knight, D.P. Dobson, W.G. Marshall, G.D. Price, J. Brodholt, Thermal expansion and crystal structure of cementite, Fe_3C, between 4 and 600 K determined by time-of-flight neutron powder diffraction. J. Appl. Cryst. **37**, 82–90 (2004). https://doi.org/10.1107/S0021889803024695
64. Y. Yin, K. Zhai, B. Zhang, S. Zhai, Electrical resistivity of iron phosphides at high- pressure and high-temperature conditions with implications for lunar core's thermal conductivity. J. Geophys. Res. Solid Earth **124**(6), 5544–5556 (2019). https://doi.org/10.1029/2018JB017157
65. E. Fruchart, A.M. Triquet, R. Fruchart, Magnetic studies of borophosphides of iron, $Fe_3B_xP_{1-x}$ ε and $ε_1$: Notes on the metal bonds of the metal transitive-metalloid in these compounds. Ann. Chim. (Paris) **9**(7–8), 323–332 (1964)

Terms and Conditions

Springer Nature journal content, brought to you courtesy of Springer Nature Customer Service Center GmbH (“Springer Nature”).
Springer Nature supports a reasonable amount of sharing of research papers by authors, subscribers and authorised users (“Users”), for small-scale personal, non-commercial use provided that all copyright, trade and service marks and other proprietary notices are maintained. By accessing, sharing, receiving or otherwise using the Springer Nature journal content you agree to these terms of use (“Terms”). For these purposes, Springer Nature considers academic use (by researchers and students) to be non-commercial.
These Terms are supplementary and will apply in addition to any applicable website terms and conditions, a relevant site licence or a personal subscription. These Terms will prevail over any conflict or ambiguity with regards to the relevant terms, a site licence or a personal subscription (to the extent of the conflict or ambiguity only). For Creative Commons-licensed articles, the terms of the Creative Commons license used will apply.
We collect and use personal data to provide access to the Springer Nature journal content. We may also use these personal data internally within ResearchGate and Springer Nature and as agreed share it, in an anonymised way, for purposes of tracking, analysis and reporting. We will not otherwise disclose your personal data outside the ResearchGate or the Springer Nature group of companies unless we have your permission as detailed in the Privacy Policy.
While Users may use the Springer Nature journal content for small scale, personal non-commercial use, it is important to note that Users may not:

1. use such content for the purpose of providing other users with access on a regular or large scale basis or as a means to circumvent access control;
2. use such content where to do so would be considered a criminal or statutory offence in any jurisdiction, or gives rise to civil liability, or is otherwise unlawful;
3. falsely or misleadingly imply or suggest endorsement, approval , sponsorship, or association unless explicitly agreed to by Springer Nature in writing;
4. use bots or other automated methods to access the content or redirect messages
5. override any security feature or exclusionary protocol; or
6. share the content in order to create substitute for Springer Nature products or services or a systematic database of Springer Nature journal content.

In line with the restriction against commercial use, Springer Nature does not permit the creation of a product or service that creates revenue, royalties, rent or income from our content or its inclusion as part of a paid for service or for other commercial gain. Springer Nature journal content cannot be used for inter-library loans and librarians may not upload Springer Nature journal content on a large scale into their, or any other, institutional repository.
These terms of use are reviewed regularly and may be amended at any time. Springer Nature is not obligated to publish any information or content on this website and may remove it or features or functionality at our sole discretion, at any time with or without notice. Springer Nature may revoke this licence to you at any time and remove access to any copies of the Springer Nature journal content which have been saved.
To the fullest extent permitted by law, Springer Nature makes no warranties, representations or guarantees to Users, either express or implied with respect to the Springer nature journal content and all parties disclaim and waive any implied warranties or warranties imposed by law, including merchantability or fitness for any particular purpose.
Please note that these rights do not automatically extend to content, data or other material published by Springer Nature that may be licensed from third parties.
If you would like to use or distribute our Springer Nature journal content to a wider audience or on a regular basis or in any other manner not expressly permitted by these Terms, please contact Springer Nature at

onlineservice@springernature.com